OPEN ACCESS
Journal of Innovative Optical Health Sciences
Vol. 17, No. 2 (2024) 2350022 (8 pages)

DOI: 10.1142/S1793545823500220

World Scientific
www.worldscientific.com

Three-dimensional morphological and fluorescent imaging of zebrafish with a continuous-rotational light-sheet microscope

Dongmin Zhang*,†, Guang Yang†, Yao Tan†, Chong Chen*, Jie Zhang† and Hui Li*,†,‡

*School of Biomedical Engineering (Suzhou)
Division of Life Sciences and Medicine
University of Science and Technology of China
Hefei 230041, P. R. China

†Suzhou Institute of Biomedical Engineering and Technology
Chinese Academy of Sciences
Suzhou, Jiangsu 215163, P. R. China
‡hui.li@sibet.ac.cn

Received 11 May 2023
Accepted 12 July 2023
Published 19 August 2023

Light-sheet fluorescence microscopy (LSFM) has been widely used to image the three-dimensional (3D) structures and functions of various millimeter-size bio-specimen such as zebrafish. However, the sample adsorption and scattering cause shading of the light-sheet illumination, preventing the even 3D image of thick samples. Herein, we report a continuous-rotational light-sheet microscope (CR-LSM) that enables simultaneous 3D bright-field and fluorescence imaging. With a high-accuracy rotational stage, CR-LSM records the outline projections and the fluorescent images of the sample at multiple rotation angles. Then, 3D morphology and fluorescent structure were reconstructed with a developed algorithm. Using CR-LSM, zebrafish's whole-fish contour and blood vessel structures were obtained simultaneously.

Keywords: Light-sheet microscope; zebrafish blood vessels; morphology.

1. Introduction

Zebrafish has been extensively used in developmental biological research as a vertebrate model organism with many advantages, such as short development cycle, and body transparency.[1,2] Given that zebrafish share 87% gene homology with humans, their developmental process offers a valuable reference for understanding the mechanisms of human embryonic development and identifying abnormal disease conditions. Using zebrafish as a model

‡Corresponding author.

organism to study vascular development has led to many discoveries of vessel growth-regulating mechanisms.[3–7] Young and Weinstein studied and evaluated the resemblance and variations of zebrafish development to other vertebrates utilizing confocal laser scanning microscopy (CLSM) to image zebrafish blood vessels.[6] In these studies, imaging of the zebrafish vasculature as well as the morphology was usually required.

Many imaging technologies have been developed to obtain the zebrafish morphology and its blood vessels, nerves or organ structures. The bright-field microscopy (BFM) was generally used to obtain morphological information.[8] The vessel structure can be obtained by fluorescence imaging techniques such as CLSM,[9] two-photon laser scanning fluorescence microscopy (2PLSM),[10,11] or light-sheet fluorescence microscopy (LSFM).[12–15] The CLSM and 2PLSM can acquire high-resolution fluorescent images via point scanning, but high phototoxicity and photobleaching were observed in the imaging process. Recently developed LFSM used two perpendicular positioned objectives to illuminate the sample and take fluorescent images. Since the sample only on the focused plane was illuminated during imaging, it significantly diminished the phototoxicity, photobleaching, and out-of-focus signals.[14,16] These advantages make LSFM an ideal tool for three-dimensional (3D) imaging samples *in vivo*.

However, when the sample is illuminated from one side, the scattering and absorption of light will induce shading, decreasing the image quality in the area away from illumination.[16] Subsequently, multidirectional LSFM was developed to obtain a clear image by fusing the 3D images at different angles.[17,18] By consecutively illuminating the sample from opposing directions, the shading of the light sheet is effectively compensated. Additionally, using dual-illumination and dual-detection approaches, the images from different views are computationally merged, resulting in a superior image. However, this multi-objective light-sheet imaging configuration has a complex structure and requires precise optical alignment.[19–21]

Herein, we report a continuous-rotational light-sheet microscope (CR-LSM) to simultaneously acquire morphology and fluorescence on zebrafish. The CR-LSM combines BFM and LSFM to obtain the sample's morphological and fluorescent signals. With the rotation of the sample stage, images from various view angles were obtained. An image process algorithm was developed to reconstruct the 3D models using the two-dimensional (2D) bright-field and fluorescent images. The reconstructed 3D structures have even imaging without shading. Using CR-LSM, the 3D model of morphology and blood vessels were reconstructed for zebrafish larvae from 2.5 days postfertilization (dpf) to 5.5 dpf.

2. Materials and Methods

2.1. *The CR-LSM setup*

Our CR-LSM features two illumination paths arranged perpendicular to each other: bright-field illumination and light-sheet illumination (Fig. 1(a)). For the light-sheet illumination, a 488 nm laser beam was collimated with three biconvex lenses (LB1471, LB1901, and LB1904, Thorlabs, USA) and modulated with a pair of mirrors, a dual-axis scanning galvo system, a biconvex lens (LB1596, Thorlabs, USA), and an illumination objective (10×, NA 0.3, water immersion, Nikon, Japan).

The illumination beam was roster-scanned in the x- and y-directions by two galvo mirrors (QS7X-Y3 and QS7Y-Y3, Thorlabs, USA), respectively. Bright-field illumination was achieved using a liquid-core fiber coupled with a light source (U-HGLGPS, Olympus, Japan) and a biconvex lens (LB1901, Thorlabs, USA). The detection path includes an objective (4×, NA 0.13, Nikon, Japan), a tube lens (TTL180-A, Thorlabs, USA), and a scientific complementary metal oxide semiconductor (sCMOS) camera (Teledyne Photometrics, Prime 95B, USA).

The rotational module consisted of a precise 2D translation mount (Thorlabs, LM1XY, SM1, USA), motorized rotation stage (Thorlabs, PRM1Z8, USA), and a machined part including SM1 external screw thread and a through hole. The machined part connected a 3 mm outer diameter glass tube and a precision 2D translation mount (Fig. 1(b)). The precision translation mount was added to adjust the position of the glass tube. Then, these connected parts were then fixed on the rotation stage. The glass tube containing samples was then placed into the designed sample pool (Fig. 1(c)). The actual layout of the imaging system is shown in Fig. 1(d).

2.2. *Resolution calibration with fluorescent beads*

Before imaging the zebrafish sample, the sample of fluorescent beads was used to calibrate the

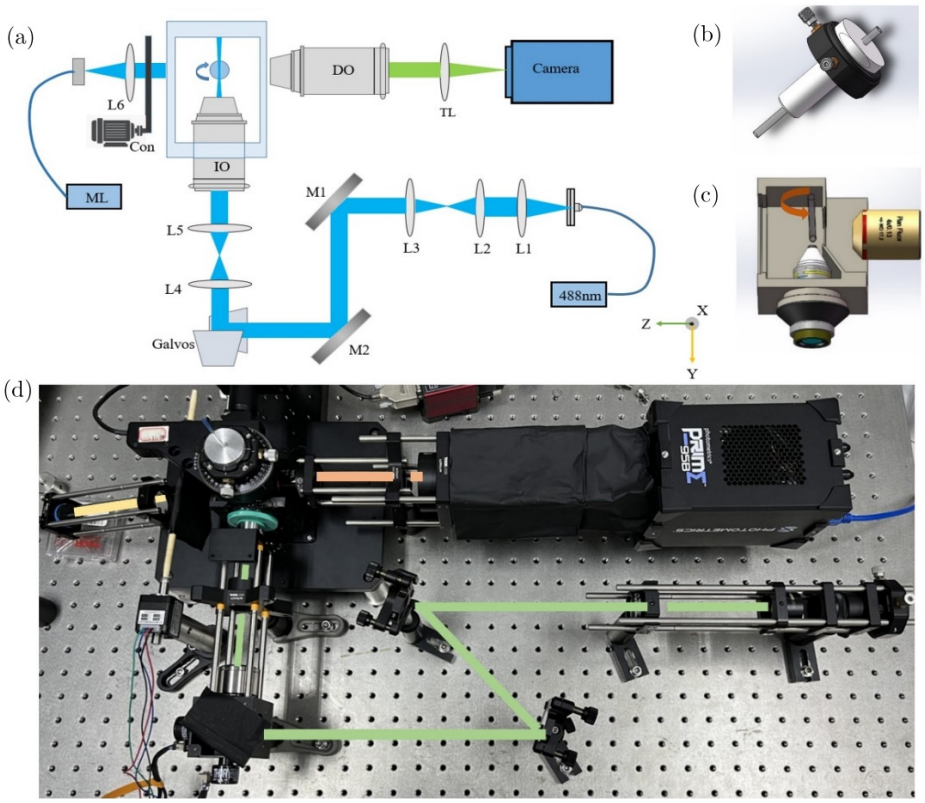

Fig. 1. Schematic representations of the CR-LSM system with bright-field and light-sheet illuminations. (a) The schematic representation of the CR-LSM optics contains two illumination paths and a detection path. L1–L6: Lenses; M1 and M2: Mirrors; Galvos: Galvo mirror pairs; IO: Illumination objective; ML: Mercury lamp; Con: Light controller; DO: Detective objective; TL: Tube lens. (b) The rotational module for sample rotation. (c) The sample pool keeping the sample in an appropriate environment. (d) Real layout of the CR-LSM system.

resolution of our imaging system. A 2 mm inner diameter glass tube was filled with 500 nm fluorescent beads (F8813-505/515 500 nm, Life Technology, USA) diluted for 80,000 times with 1% low-melting point agarose (Sea Plaque GTG Agarose, Lonza, Switzerland). To determine the rotation axes of these 2D images, a small plastic cylinder was put into the glass tube as a marker. Then, the rotational axes of these images were determined using the marker.

The glass tube containing fluorescent beads and the maker was assembled on the rotation stage. Then, the agarose cylinder was pushed out from the glass tube for imaging. By combining the optical imaging technologies of LSFM and BFM, the CR-LSM captured a sequence of bright-field and fluorescent 2D images from different view angles. During the experiment, fluorescent and bight-field images were captured after rotating the sample for 2° with the rotation module. Then, 180 2D bright-field and fluorescent images were captured while rotating the samples in a circle. The bright-field signals were used to precisely determine each image's rotation axes position, as elaborated in Sec. 2.4.

2.3. *Zebrafish culture and imaging*

Transgenic (fli1:EGFP) zebrafishes were maintained at ∼28°C in a 14 h light:10 h dark environment. First, the embryos were raised in a culture medium (1.2 g sea salt per 20 L purified water) for 24 h postfertilization (hpf). Then, embryos were transferred to a 1-phenyl-2-thiourea (PTU 0.0045% P7629, Sigma, USA) medium to inhibit pigment formation. In 2.5 dpf, zebrafish larvae were obtained for imaging. The zebrafish conducted following the National Institutes of Health guide for the care and use of laboratory animals (NIH Publications No. 8023, revised 1978), and were approved by the animal ethics committee of the Suzhou Institute of Biomedical Engineering and Technology, CAS.

Before imaging, zebrafish larvae were anesthetized by adding 0.4% tricaine solution (A5040, Sigma, USA) on a ratio of 1:25. After that, one zebrafish was picked out and embedded in the 2 mm inner diameter glass tube filled with 1% low-melting point agarose. Then, the imaging process was performed similarly to that of fluorescent bead samples. Here, no extra marker was needed to determine the rotation axes of each image. These resulting images were then used for morphology and blood vessels reconstruction. For bright-field and fluorescent imaging, the exposure time of camera is 2 ms and 60 ms, respectively. The imaging system contains a rotation module and a bright-field controller, which consuming lots of time during the imaging process. It takes about 2 min to capture 360 morphology and blood vessels images of zebrafish.

2.4. *3D image reconstruction of CR-LSM*

After imaging the fluorescent beads, we obtained 180 bright-field images and 180 fluorescent images at a 2° step. Then, the rotation axes of these 360 images could be calculated using the 180 bright-field images. We first symmetrically flipped the bright-field images at the view angle of 180° with respect to the central axis of the image. Then, the image at the view angle of 0° was matched with the flipped image at the view angle of 180° based on the marker, and the displacement of the two images was calculated during the matching (Fig. 2(a)). Hence, the rotation axes of the bright-field images at the view angle of 0° and 180° could be found. With the same theory above, the bright-field images at the view angle from 0° to 178° were matched with the images at the view angle from 180° to 358° one by one. All the rotation axes of every image, including the fluorescent images, were calculated. The region of interest (ROI) of the 180 fluorescent images was cropped out according to their rotation axes. The rotation axes of the cropped images coincided with their corresponding center axes.

In reconstructing 3D models, we mapped the pixels of each rotational image stack to the 3D space. As shown in Fig. 2(b), $p(\rho, z, \alpha)$ was assumed as the coordinate of 2D image pixels at the view angle of α, ρ, and z, respectively, represent the distances between the pixel and the centerline and bottom of the image. $P(X, Y, Z)$ was assumed as the 3D coordinate of p. With these definitions, equations for the transformation of p to P described as follows:

$$X = \rho \cdot \cos(\alpha), \tag{1}$$

$$Y = \rho \cdot \sin(\alpha), \tag{2}$$

$$Z = z. \tag{3}$$

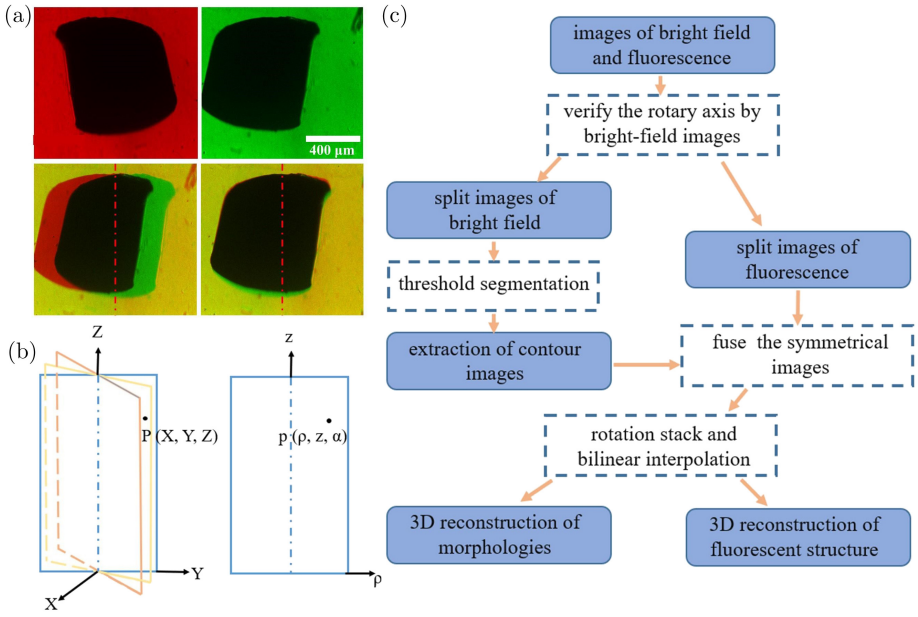

Fig. 2. The principle and process of the 3D reconstruction algorithm. (a) The principle of the 3D reconstruction algorithm. (b) The process of determining the rotation axes for every image. (c) The 3D reconstruction workflow of bright-field and fluorescence models.

Finally, the bilinear interpolation algorithm was used to calculate the gray value of the adjacent 3D spatial pixels.[22] Based on the workflow shown in Fig. 2(c), we had reconstructed the 3D models of fluorescent and morphological of the sample.

3. Results

3.1. *Resolution calibration*

To calibrate the resolution of CR-LSM, the 3D model of 500 nm fluorescent beads was reconstructed using the developed imaging system. As illustrated in the previous section, the bright-field images were captured to determine the rotation axes of images at different view angles.

In reconstructing the 3D model of fluorescent beads, the fluorescent images at angle view of θ° and $180^\circ + \theta^\circ$ were merged into one image for that the two corresponding images were captured from the same section of the sample. After that, we mapped the pixels of each rotational image to the 3D space by using the above-mentioned method. As a result, the 3D model of fluorescent beads got reconstructed with the process of bilinear interpolation algorithm.[22]

The 3D model of the fluorescent beads was evenly divided into four parts to evaluate the imaging quality (Fig. 3(a)). The mean intensity of all pixels for these four parts were 108.4, 107.5, 110.2, and 108.8. The maximum intensity difference between these four parts was 2.7. After that, the resolution of the imaging system was evaluated by measuring the full width at half maximum (FWHM) of randomly selected fluorescent beads at different positions. The resolution in the tangential direction decreases gradually along the direction of far away from the rotation axis, while the resolution in the radial direction remains about 10 μm (Fig. 3(d)). Hence, CR-LSM provides an even imaging without shading.

In light-sheet microscope, as the thickness of the light sheet increases along the propagation direction, its axial resolution also decreases. The axial resolution of the optical system can be estimated by the FWHM of the point spread function (PSF) in the axial direction (z).[23] Hence, the variation in axial resolution at various locations from the center of the light sheet can be calculated (Fig. 4(d)), which is approximately close to the results of the experiment.

3.2. *3D image reconstruction of zebrafish*

In imaging zebrafish, one bright-field image and one fluorescent image were captured for every 2° using the developed imaging system. These 360 2D images were used to reconstruct the 3D models of zebrafish morphology and blood vessels. Likes reconstructing

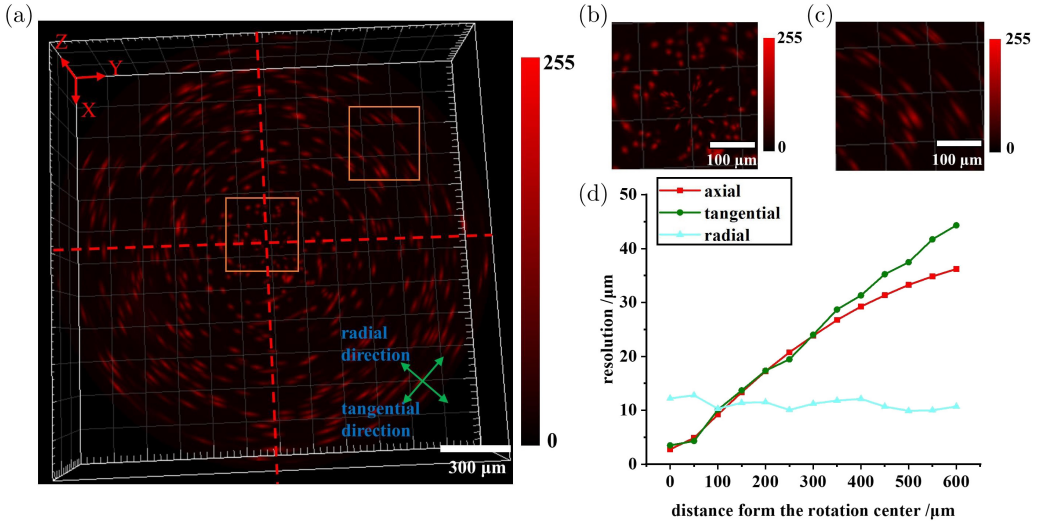

Fig. 3. (Color online) Calibration results of the CR-LSM using the reconstructed 3D model of fluorescent beads. (a) Reconstructed 3D model of the fluorescent beads. (b), (c) Enlarged area of orange boxes in (a). (d) The red polyline represents the theoretically calculated axial resolution results at various positions of the light sheet, the remaining two polylines representing the tangential and radial calibrated resolution results of our imaging system.

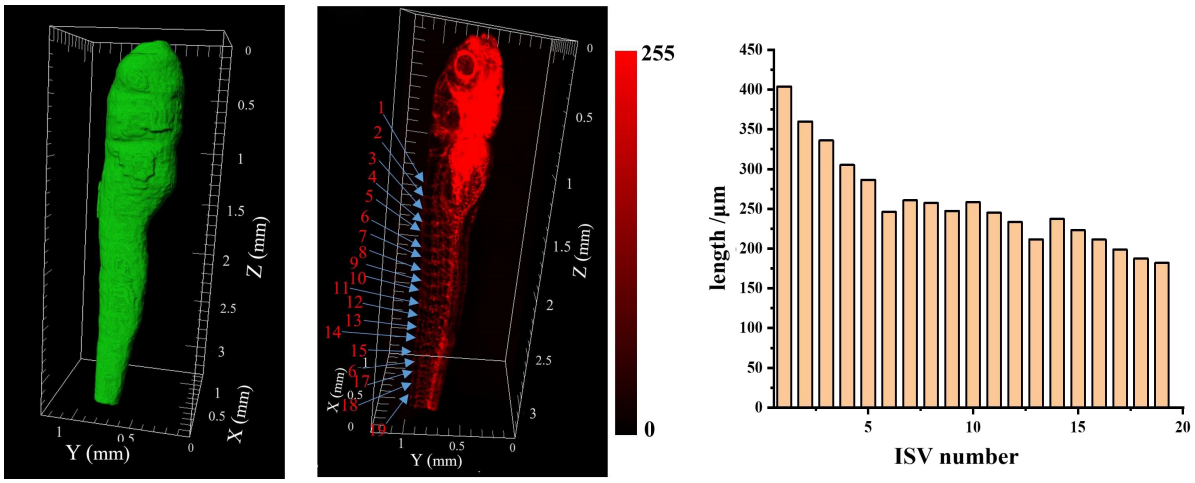

(a) (b) (c)

Fig. 4. Reconstructed 3D models of the zebrafish morphology and blood vessels. (a) Reconstructed 3D model of zebrafish morphology. (b) Reconstructed 3D model of zebrafish blood vessels. (c) The lengths of 19 ISV labeled in (b).

of fluorescent beads, the rotation axes were determined using the 180 bright-field images of zebrafish, and ROI was cropped out from the bright-field and fluorescent images with respect to their corresponding axes. Next, the vascular images in the view angel of θ° and $180^\circ + \theta^\circ$ were merged. Then, every pixel of these 90 vascular images was mapped to the corresponding 3D space, and the 3D model was reconstructed using the bilinear interpolation algorithm.[22]

In reconstructing the 3D model of zebrafish morphology, we used 36 evenly spaced cropped bright-field images. First, we normalized the bright-field images, and performed threshold segmentation to obtain the outline of the zebrafish. Similarly, these 36 images were merged into 18 images. Each pixel of these 18 images was mapped into 3D space. Finally, the bilinear interpolation algorithm was used to fill the gaps between the adjacent pixels. The 3D model of zebrafish morphology is shown in Fig. 4(a). The reconstructed 3D model of zebrafish blood vessels is shown in Fig. 4(b). With the 3D models, the estimated volume of the zebrafish to be $\sim 0.45\,\text{mm}^3$. The lengths of 19 intersegmental vessels (ISV) of the zebrafish in 5.5 dpf were measured (Fig. 4(c)).

3.3. *Morphology and ISV development of zebrafish from 2.5 dpf to 5.5 dpf*

When zebrafishes are used for cardiovascular disease and drug screening studies, their interactions to drugs can be inferred from the vascular development. Therefore, measuring the volumes and lengths of different blood vessels is of great significance. Then, we imaged zebrafish vessels with the developed imaging system at seven different developmental stages ranging from 2.5 dpf to 5.5 dpf. Three ISV were randomly selected for developmental studies of zebrafish blood vessels (Fig. 5(a–b)). For the zebrafish from 2.5 dpf to 5.5 dpf, the ratio in the volume of the vessels between the second and eleventh ISV and its corresponding volume of the body part were counted (Fig. 5(c)). The ratio of the volume occupied by blood vessels gradually leveled off after increasing to $\sim 12\%$. The lengths of these randomly selected vessels in different developmental stages of the zebrafish were measured (Fig. 5(d)). The growth rate of the second ISV is much slower than that of the eighth and eleventh. We concluded that the CR-LSM greatly reduces the effect of light scattering and absorption, providing an even 3D model compared with the traditional LSFM. These results indicated that CR-LSM could not only obtain the morphological and fluorescent imaging of zebrafish, but also ameliorate the drawbacks of the LSFM.

4. Discussion

Our developed CR-LSM can simultaneously obtain bright-field and fluorescence information to reconstruct the sample's 3D morphology and structures. In the studies of zebrafish blood vessel

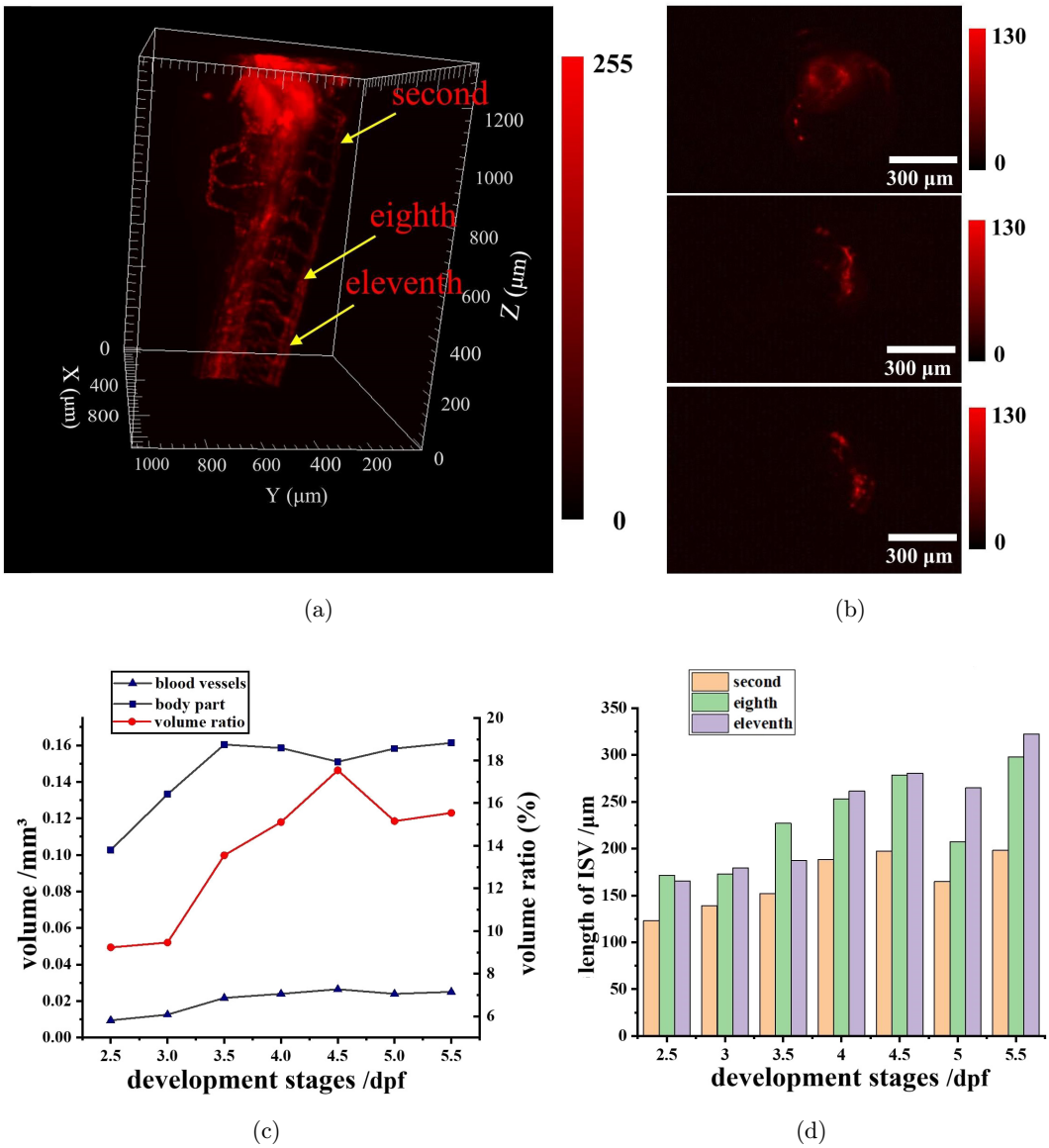

Fig. 5. Analysis of vascular development of zebrafish. (a) 3D model of partial vessels in zebrafish. (b) The slice images of Fig. 4(a) at the three positions of selected ISV. (c) The volume of the vessels, body part and their corresponding ratio between the second and eleventh ISV. (d) Three randomly selected ISV lengths of zebrafish at different developmental stages.

developments, aligned vessel structures with body morphology enables researchers to do more comprehensive analysis. The 3D images were reconstructed from multiple sectioned images with continuous sample rotation. Hence, CR-LSM can effectively solve the shading problem in traditional light-sheet microscopy and produce even 3D images. Using our CR-LSM the 3D fluorescent model can be reconstructed with 180 2D fluorescent images. The resolution in the radial direction remains about 10 μm. With a range of 250 μm from the imaging center, the resolution in the tangential direction is within 20 μm.

The current CR-LSM can still be optimized in several aspects for better imaging performance. First, the rotation module, camera, and light sources can be synchronized by hardware triggering to improve imaging speed. Second, a rotation stage with higher accuracy and stability would simplify the alignment process and decrease the drift during long time imaging. Third, the resolution change along the tangential direction can be resolved by scanning a Bessel beam to form a light sheet with same thickness within the field of view. With these improvements, the CR-LSM can not only improve imaging efficiency, but also solve the problem of

resolution changes in the tangential direction and achieve isotropic imaging. We anticipate that CR-LSM can be applied to characterize long-time developments of different zebrafish organs and quantitatively evaluate the effects of various drugs.

5. Conclusions

In summary, we developed a multimodal 3D imaging platform CR-LSM to obtain even images of bright field and fluorescence. The reconstructed models by our CR-LSM can help researchers to do more detailed studies about biological development and drug discovery. The system can be easily extended to image other millimeter-sized models, such as *Caenorhabditis elegans* and organoids.

Acknowledgments

The authors acknowledged the National Natural Science Foundation of China (62205368); the Key Research and Development Program of Jiangsu Province (BE2020664).

Conflicts of Interest

The authors declare that there are no conflicts of interest relevant to this article.

References

1. S. A. Brittijn *et al.*, "Zebrafish development and regeneration: New tools for biomedical research," *Int. J. Dev. Biol.* **53**, 835–850 (2009).
2. A. V. Gore *et al.*, "Vascular development in the zebrafish," *Cold Spring Harb. Perspect. Med.* **2**, a006684 (2012).
3. D. Li *et al.*, "VCAM-1+ macrophages guide the homing of HSPCs to a vascular niche," *Nature* **564**, 119–124 (2018).
4. B. M. Hogan, S. Schulte-Merker, "How to plumb a pisces: Understanding vascular development and disease using zebrafish embryos," *Dev. Cell* **42**, 567–583 (2017).
5. S. Isogai, M. Horiguchi, B. M. Weinstein, "The vascular anatomy of the developing zebrafish: An atlas of embryonic and early larval development," *Dev. Biol.* **230**, 78–301 (2001).
6. R. C. Young, B. M. Weinstein, "Visualization and experimental analysis of blood vessel formation using transgenic zebrafish," *Birth Defects Res. C Embryo Today* **81**, 86–296 (2007).
7. P. J. Keller *et al.*, "Digital scanned laser light-sheet fluorescence microscopy (DSLM) of zebrafish and drosophila embryonic development," *Cold Spring Harb. Protoc.* **2011**, 1235–1243 (2011).
8. O. A. Osibote *et al.*, "Automated focusing in bright-field microscopy for tuberculosis detection," *J. Microsc.* **240**, 155–163 (2010).
9. R. Alvarez-Román *et al.*, "Visualization of skin penetration using confocal laser scanning microscopy," *Eur. J. Pharm. Biopharm.* **58**, 301–316 (2004).
10. R. Niesner *et al.*, "The power of single and multi-beam two-photon microscopy for high-resolution and high-speed deep tissue and intravital imaging," *Biophys. J.* **93**, 2519–2529 (2007).
11. F. Helmchen, W. Denk, "Deep tissue two-photon microscopy," *Nat. Methods* **2**, 932–940 (2005).
12. O. E. Olarte *et al.*, "Light-sheet microscopy: A tutorial," *Adv. Opt. Photonics* **10**, 111–179 (2018).
13. F. O. Fahrbach *et al.*, "Rapid 3D light-sheet microscopy with a tunable lens," *Opt. Express* **21**, 21010–21026 (2013).
14. E. H. K. Stelzer *et al.*, "Light sheet fluorescence microscopy," *Nat. Rev. Methods Primers* **1**, 73 (2021).
15. M. Weber, J. Huisken, "Light sheet microscopy for real-time developmental biology," *Curr. Opin. Genet. Dev.* **21**, 566–572 (2011).
16. U. Krzic *et al.*, "Multiview light-sheet microscope for rapid *in toto* imaging," *Nat. Methods* **9**, 730–733 (2012).
17. J. Huisken, D. Y. Stainier, "Even fluorescence excitation by multidirectional selective plane illumination microscopy (mSPIM)," *Opt. Lett.* **32**, 2608–2610 (2007).
18. R. Tomer *et al.*, "Quantitative high-speed imaging of entire developing embryos with simultaneous multiview light-sheet microscopy," *Nat. Methods* **9**, 755–763 (2012).
19. Z. Yang *et al.*, "A compact Airy beam light sheet microscope with a tilted cylindrical lens," *Biomed. Opt. Express* **5**, 3434–3442 (2014).
20. T. Vettenburg *et al.*, "Light-sheet microscopy using an Airy beam," *Nat. Methods* **11**, 541–544 (2014).
21. B. C. Chen *et al.*, "Lattice light-sheet microscopy: Imaging molecules to embryos at high spatiotemporal resolution," *Science* **346**, 1257998 (2014).
22. K. A. Kalpoma, K. Kawano, "IKONOS image fusion process using steepest descent method with bi-linear interpolation," *Int. J. Remote Sens.* **34**, 505–518 (2013).
23. W. Zong *et al.*, "Large-field high-resolution two-photon digital scanned light-sheet microscopy," *Cell Res.* **25**, 254–257 (2015).